Title
Resonant domain-wall-enhanced tunable microwave ferroelectrics.

Journal
Nature, 560(7720)

ISSN
0028-0836

Authors
Gu, Zongquan
Pandya, Shishir
Samanta, Atanu
et al.

Publication Date
2018-08-01

DOI
10.1038/s41586-018-0434-2

Peer reviewed

LETTER

https://doi.org/10.1038/s41586-018-0434-2

Resonant domain–wall–enhanced tunable microwave ferroelectrics

Zongquan Gu[1,2], Shishir Pandya[3], Atanu Samanta[4], Shi Liu[5], Geoffrey Xiao[1], Cedric J. G. Meyers[6], Anoop R. Damodaran[3], Haim Barak[4], Arvind Dasgupta[3], Sahar Saremi[3], Alessia Polemi[1], Liyan Wu[7], Adrian A. Podpirka[1], Alexandria Will-Cole[1], Christopher J. Hawley[1], Peter K. Davies[7], Robert A. York[6], Ilya Grinberg[4], Lane W. Martin[3,8] & Jonathan E. Spanier[1,2,9]*

Ordering of ferroelectric polarization[1] and its trajectory in response to an electric field[2] are essential for the operation of non-volatile memories[3], transducers[4] and electro-optic devices[5]. However, for voltage control of capacitance and frequency agility in telecommunication devices, domain walls have long been thought to be a hindrance because they lead to high dielectric loss and hysteresis in the device response to an applied electric field[6]. To avoid these effects, tunable dielectrics are often operated under piezoelectric resonance conditions, relying on operation well above the ferroelectric Curie temperature[7], where tunability is compromised. Therefore, there is an unavoidable trade-off between the requirements of high tunability and low loss in tunable dielectric devices, which leads to severe limitations on their figure of merit. Here we show that domain structure can in fact be exploited to obtain ultralow loss and exceptional frequency selectivity without piezoelectric resonance. We use intrinsically tunable materials with properties that are defined not only by their chemical composition, but also by the proximity and accessibility of thermodynamically predicted strain-induced, ferroelectric domain-wall variants[8]. The resulting gigahertz microwave tunability and dielectric loss are better than those of the best film devices by one to two orders of magnitude and comparable to those of bulk single crystals. The measured quality factors exceed the theoretically predicted zero-field intrinsic limit owing to domain-wall fluctuations, rather than field-induced piezoelectric oscillations, which are usually associated with resonance. Resonant frequency tuning across the entire L, S and C microwave bands (1–8 gigahertz) is achieved in an individual device—a range about 100 times larger than that of the best intrinsically tunable material. These results point to a rich phase space of possible nanometre-scale domain structures that can be used to surmount current limitations, and demonstrate a promising strategy for obtaining ultrahigh frequency agility and low-loss microwave devices.

Current telecommunication devices rely on our ability to tune the device frequency in the radiofrequency spectrum. The development of bulk- and thin-film-based acoustic wave filters, resonators and other devices over the last few decades has allowed cell phone miniaturization, antenna tuning and the development of current mobile telecommunication technology. Further advancement (for example, 5G and IoT technologies) requires an even more efficient use of the spectrum, necessitating the development of thin-film dielectrics with higher dielectric tunability, n, quality factor, Q, and figures of merit, motivating intense research and development efforts. In particular, extrinsic effects, such as defects, strain, interface and polar ordering, have been intensely investigated and recent advances have enhanced our understanding of how functional properties can be tailored, can evolve from symmetry breaking or can even be induced artificially[9–12]. Extrinsic enhancement of susceptibility from ferroelectric domain walls[13] can be attained by strain engineering through the creation of domain-wall-rich films, whose extrinsic character allows dielectric properties not bounded by the intrinsic limits of the defect-free bulk. Nevertheless, for tunable dielectrics, polar domains have not been considered helpful and are generally equivalent to other crystal imperfections (for example, oxygen vacancies) that must be suppressed to achieve greater material quality and thus lower dielectric loss and higher figure-of-merit values[14]. Therefore, domain engineering has not been investigated for tunable dielectrics.

In this work, we investigated the dielectric response of strained $Ba_xSr_{1-x}TiO_3$ (BST) films in the vicinity of the Curie temperature, T_C. The nearly isotropic free-energy–polarization landscape (and lower barrier to polarization rotation) of these materials is expected to lead to a rich phase diagram and a large response to an applied electric field.

Thermodynamic Ginzburg–Landau–Devonshire (GLD) model calculations support the hypothesis that large in-plane permittivity values can be obtained via in-plane domains. Application of the phenomenological GLD model permits calculation of in-plane strain (u_s)–temperature (T)–polarization ($\boldsymbol{P}$) phase diagrams and of the dielectric permittivity (Fig. 1; see Methods and Supplementary Information), with a number of additional domain variants ('superdomain' phases[15]) predicted for BST films (Fig. 1a–g; Methods and Supplementary Information). We focus on BST with $x = 0.8$, whose phase diagram exhibits a vertex, where a number of domain-wall-variant phases are predicted to intersect near room temperature (Fig. 1a; red circle). On the basis of the close proximity and high accessibility of the different variants, we refer to this region of the phase diagram as a manifold-domain-wall-variant material (MDVM). Zero- and finite-field phase-field model calculations for three selected strain states (denoted in Fig. 1a by the yellow dashed lines I, II and III) confirm the expected c^+/c^- structure for a compressively strained film (I) and an in-plane domain structure for a film under moderate tensile strain (III) (Fig. 1a). Application of a moderately large field (0.1 MV cm^{-1} along [100]) leaves the domain structure in I (Fig. 1b) and III (Fig. 1f) essentially unchanged (Fig. 1c, g). For case II, which corresponds to the MDVM material, the aa_1/aa_2 domain-wall-variant structure at zero field (Fig. 1d) is predicted, suggesting the coexistence of multiple domain-wall variants, which is consistent with the material's location in the phase diagram. Despite the softer three-dimensional potential-energy landscape of II compared with those of I and III, the domain structure is not eliminated at moderate fields (Fig. 1e), consistent with reports on epitaxial films in which domain structures cannot be eliminated[16] under an applied electric field.

We find that the dielectric permittivity values for the MDVM-engineered films exceed the composition-specific state of the art for dielectric thin films: theoretically predicted values for zero-field

[1]Department of Materials Science and Engineering, Drexel University, Philadelphia, PA, USA. [2]Department of Electrical and Computer Engineering, Drexel University, Philadelphia, PA, USA. [3]Department of Materials Science and Engineering, University of California at Berkeley, Berkeley, CA, USA. [4]Department of Chemistry, Bar-Ilan University, Ramat-Gan, Israel. [5]Carnegie Institution for Science, Washington, DC, USA. [6]Department of Electrical and Computer Engineering, University of California at Santa Barbara, Santa Barbara, CA, USA. [7]Department of Materials Science and Engineering, University of Pennsylvania, Philadelphia, PA, USA. [8]Materials Sciences Division, Lawrence Berkeley National Laboratory, Berkeley, CA, USA. [9]Department of Physics, Drexel University, Philadelphia, PA, USA. *e-mail: spanier@drexel.edu

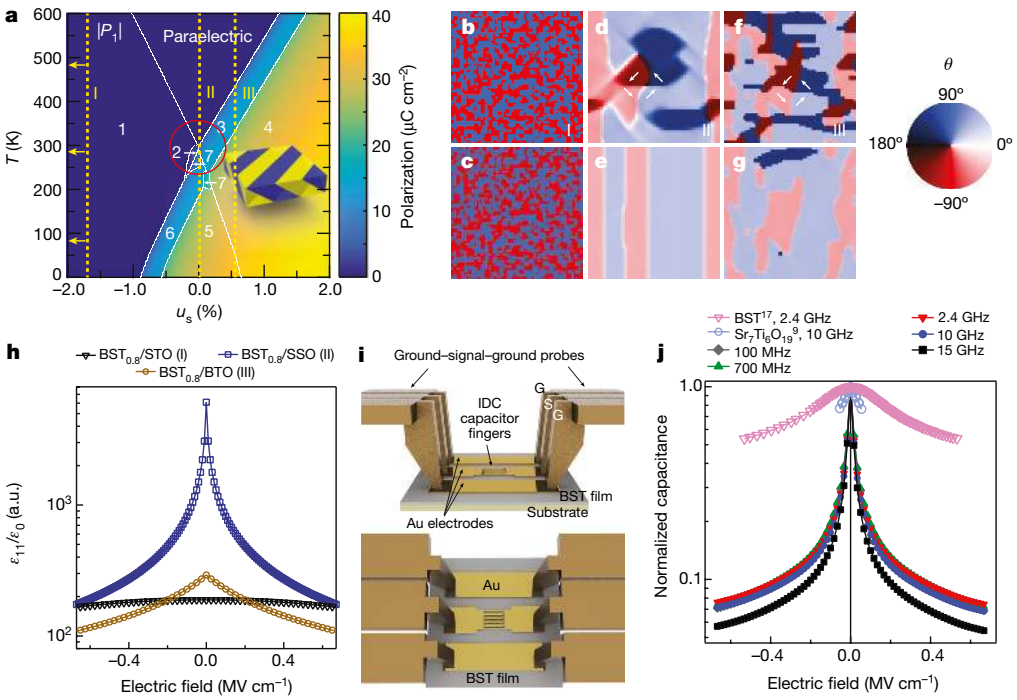

Fig. 1 | Design of a MDVM and its microwave dielectric tunability. **a**, Thermodynamic landscape of in-plane polarization favouring domain-wall variants, showing the calculated average value of in-plane polarization, $|P_1|$, as a function of temperature, T, and in-plane strain, u_s, for $Ba_{0.8}Sr_{0.2}TiO_3$. Arabic numerals denote various thermodynamically predicted domain-wall-variant structures (see Supplementary Information). Dashed lines denote the strain states I, II and III, where state I lies outside the plotted range, as indicated by the yellow arrows. White lines denote the boundaries between domain-wall-variant phases. Shown in the inset is an illustration of an example domain-wall variant, where yellow and purple colours correspond to regions of the film with different polarization directions. **b**–**g**, Phase-field simulations of domain structure for equivalent strains and corresponding non-degenerate (I and III) and degenerate (II) domain-variant phase states in $BaTiO_3$ at about 10 K < T_C under zero field (**b**, **d**, **f**) reveal high out-of-plane (**b**) and in-plane (**d**, **f**) domain-wall densities that persist even under a moderate in-plane field of 0.1 MV cm^{-1} applied along [100] (**c**, **e**, **g**). **b**, **c**, Maps of plane-normal polarization P_3, where blue and red colours correspond to +30 μC cm^2 and −30 μC cm^2, respectively. **d**–**g**, Maps of in-plane local polarization direction, as denoted by the white arrows. θ is the angle between [100] and the sum of the two in-plane components, $P_1 + P_2$ (see Supplementary Information). **h**, The effect of proximity to this domain-phase-variant degeneracy point; displayed is the theoretically predicted in-plane quasi-static-field tunability of the relative dielectric permittivity, $\varepsilon_{11}/\varepsilon_0$, in $Ba_{0.8}Sr_{0.2}TiO_3$ ($BST_{0.8}$) films on $SrTiO_3$ (STO), on $SmScO_3$ (SSO) and on $BaTiO_3$ (BTO), corresponding to strain states I, II and III, respectively, calculated using the GLD model. a.u., arbitrary units. **i**, Illustration of the experimental two-port co-planar geometry used to measure the microwave dielectric response of the BST epitaxial film (situated on the substrate), using ground (G) and source (S) input and output probes through the Au IDC finger electrodes. **j**, Measured in-plane field tuning of in-plane normalized capacitance at selected frequencies for a 400-nm-thick MDVM film sample ($Ba_{0.8}Sr_{0.2}TiO_3/SmScO_3(110)$), compared with those of epitaxial paraelectric BST[17] and $Sr_7Ti_6O_{19}$[9] films.

relative dielectric permittivity $\varepsilon_{11}/\varepsilon_0$ easily exceed 10,000, reaching 10^5 for selected combinations. Higher permittivity promotes enhanced dielectric and capacitance tunability, n ($n = \varepsilon_{r,max}/\varepsilon_{r,min} = C_{max}/C_{min}$, where ε_r is the real part of the dielectric permittivity and C_{max} and C_{min} are the capacitances at zero field and with an applied electric field E, respectively), aided by proximity to the phase boundary. The theoretically calculated quasi-static in-plane tunability of MDVM films can be remarkably large. For example, an $x = 0.8$ film coherently strained on $SmScO_3(110)$ ($u_s \approx 0.05\%$, case II) is predicted to have tunability $n(E_1) > 20$ at $E_1 = 0.3$ MV cm^{-1}, whereas for films deposited on $SrTiO_3$ (I) and $BaTiO_3$ (III) n is considerably lower (Fig. 1h).

Experimental results support the GLD theory predictions. Epitaxial $x = 0.8$ films, 100 nm and 400 nm thick, were deposited on $SmScO_3(110)$ by pulsed-laser deposition and were characterized using a variety of techniques (Methods, Supplementary Information). Compared with the bulk, the smaller out-of-plane lattice parameters in our films favour in-plane domain formation, and plane-normal and lateral dual-amplitude resonance tracking (DART) piezoresponse force microscopy confirms the presence of in-plane oriented domains, with domain walls aligned along [100] or [010], consistent with the $aa_1/aa_2/aa_1/aa_2$ domain structure (Supplementary Information). Voltage-dependent capacitance data in the co-planar geometry (Fig. 1i, Methods) at selected frequencies across the measurement range demonstrate high tunability at modest fields (Fig. 1j), in agreement with our calculations, which persists beyond 20 GHz. This tunability, even at equivalent fields, is considerably greater than the current state of the art in films grown by molecular beam epitaxy, including Ruddlesden–Popper $Sr_7Ti_6O_{19}$[9] and (Ba,Sr)TiO_3[17] (Fig. 1j). Remarkably, $n(f)$ remains greater than 13 (at 0.67 MV cm^{-1}) almost throughout the entire frequency range studied, peaking at $n \approx 18.5$ at 15.2 GHz (Supplementary Fig. 10). The deposited films also exhibit low losses (high Q values), in contrast to the high losses that usually accompany high tunabilities. MDVM films exhibit low Q at zero field, but large Q ($\overline{Q(f)} \approx 1{,}200$, frequency-averaged in 0.1–20 GHz) at maximum field. At the highest applied field, Q ranges generally between 10^2 and 10^3 over the range 2–10 GHz (Supplementary Fig. 11).

A closer examination reveals extraordinary features in thinner films: field–frequency combinations for which Q oscillates with frequency easily exceed the frequency-dependent bulk intrinsic limit for $BaTiO_3$ near T_C (less than about 10^3; Supplementary Fig. 17), reaching, and even exceeding, 10^5 (Fig. 2; Supplementary Information). These Q values are much greater than the best ones reported for intrinsically tunable film materials[17,18] (including ferroelectrics considered for high-Q dielectrics[18–20]) and greater than those of AlN films[21–24], which are the leading non-ferroelectric (that is, not intrinsically tunable) piezoelectrics. They are comparable, in fact, to values measured for bulk single-crystal quartz[25], sapphire[26] and ZnO[27]. The field dependence of the resonance frequency, $f_r(E)$, shows exceptional variation across one frequency decade, spanning the L (1–2 GHz), S (2–4 GHz) and C (4–8 GHz) bands and extending into the X band (8–12 GHz), all in a

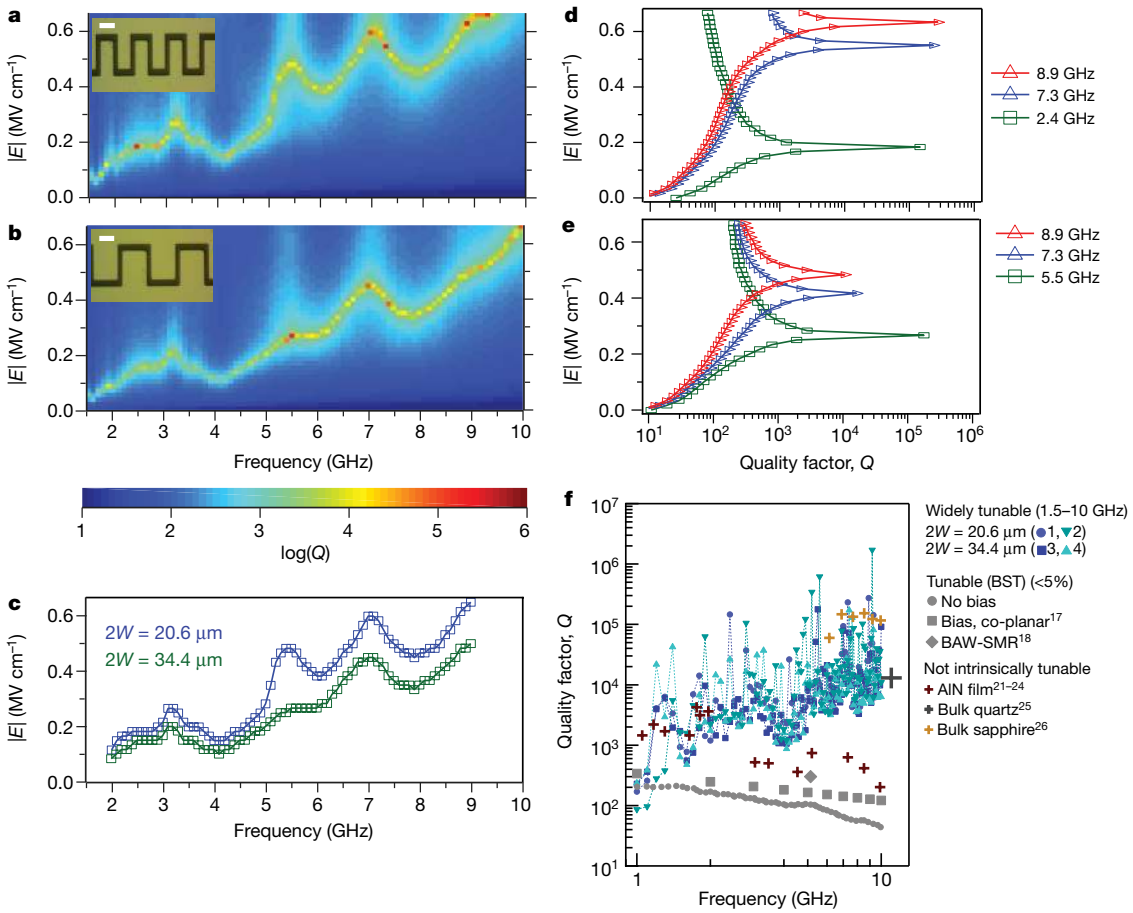

Fig. 2 | Microwave spectroscopy results revealing field-dependent resonant domain-wall spectral signatures of ultralow loss and tunable resonant performance. a, **b**, Experimentally determined Q as a function of frequency and d.c. in-plane bias field for a 100-nm-thick film with ten (**a**) and six (**b**) IDC electrode pairs. The period $2W$ is defined by the electrode finger width and the inter-electrode spacing. The insets show optical micrographs of the IDC electrode pairs (scale bar, 10 μm). **c**, Frequency and electric field values for which $Q(f)$ peaks are obtained for the devices in **a** (blue; $2W = 20.6$ μm) and **b** (green; $2W = 34.4$ μm). The plot shows that the spectra of the voltage-dependent frequencies for which the resonant $Q(f)$ peaks occur are essentially the same and that the resonant frequency can be bias-tuned by about 400%, from around 2 GHz at about 0.1 MV cm^{-1} to 10 GHz at about 0.67 MV cm^{-1}, with $10^3 \lesssim Q \lesssim 10^6$. **d**, **e**, Representative traces of d.c.-field-dependent Q at different frequencies for the devices shown in **a** and **b**, respectively. **f**, Peak Q values were collected at 100 frequencies in four distinct devices: the devices shown in **a** (1; blue circles) and **b** (3; blue squares) and two additional devices (2, 4) with the same characteristics as devices 1 and 3. The data show an increase of more than one order of magnitude over approximately one frequency decade, deviating strongly from the usual f^{-1} scaling law. Shown for comparison are the highest values reported for piezoelectric resonators made of bulk single-crystal quartz[25], sapphire[26] and AlN film[21–24], none of which is intrinsically tunable (each point represents an individual device), and values reported for intrinsically tunable BST films[17,18], including a bulk acoustic-wave solidly mounted resonator (BAW-SMR) film.

single device. The commutation quality factor[28], $\mathrm{CQF}(f) = [n(f) - 1]^2 Q(0, f)Q(E, f)/n(f)$, a key metric that incorporates $n(E)$ and $Q(E)$, shows values that are greater than those of the best reported BST films[17] (Supplementary Information).

Bulk dielectric and film resonators rely on electromechanical coupling of microwave power through piezoelectric oscillations, which appear as resonant and anti-resonant features that can be voltage-tuned by less than 4.5% in the best tunable materials[29]. Considering the change in the piezoelectric coupling coefficient, the calculated bias-field dependence of the resonance and anti-resonance frequencies of in-plane piezoelectric oscillations for $Ba_{0.8}Sr_{0.2}TiO_3$ in our experimental geometry amounts to not more than about 3% for 0–0.6 MV cm^{-1} (Supplementary Information)—hundreds of times lower than that observed in our devices. Furthermore, the design of piezoelectric resonators using in-plane piezoelectric oscillations operating at fundamental (or higher-mode) frequency relies on interdigitated capacitor (IDC) electrode periodicity[23,30]. Although we cannot rule out potential contributions from other possible mechanisms (for example, piezoelectric oscillations), devices that differ in electrode finger width yield spectra that are essentially the same (Fig. 2c), further demonstrating that it is highly unlikely that piezoelectric oscillations cause the observed spectrum.

We now investigate the origin of the unusual experimentally observed Q spikes using the data obtained from molecular dynamics simulations of a model $BaTiO_3$ (BTO) system (Methods). The analytical theory of the intrinsic dielectric response of a ferroelectric material[14] predicts a $1/f$ dependence for $Q(f)$, as is also found in our single-domain molecular dynamics simulations (Supplementary Information), indicating that the unusual f-dependence of Q is due to extrinsic effects. Examination of static dielectric response shows that the peak dielectric constant value is observed in the ferroelectric phase (Supplementary Information). Such a domain-wall-driven shift of the dielectric response peak to the ferroelectric phase was previously observed experimentally in $BaTiO_3$ in the ferroelectric phase close to T_C[13,31]. In addition, reversible domain-wall oscillations are also found to lead to the peak dielectric constant in the ferroelectric phase for the model aa_1/aa_2 domain-wall supercell in our molecular dynamics simulations (Fig. 3a, Supplementary Information). The main reason for this domain-wall contribution to the dielectric permittivity is the existence of very low-energy modes localized on the two-dimensional

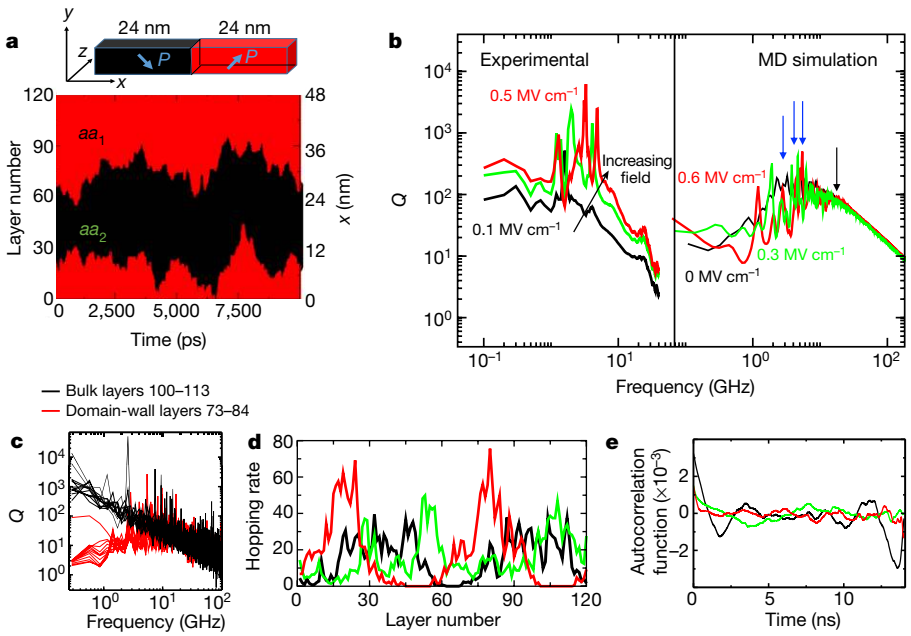

Fig. 3 | Molecular dynamics simulation of *Q*. a, Illustration of the molecular dynamics supercell and domain fluctuations at $E_x = 0.6$ MV cm^{-1}, with the $P_y > 0$ domain shown in black (domain type aa_2) and the $P_y < 0$ domain shown in red (domain type aa_1). **b**, Experimental Q (left) and Q_y obtained by molecular dynamics (MD) simulations (right) for the aa_1/aa_2 domain structure. Experimental data are shown for $E = 0.09$ MV cm^{-1} (black), $E = 0.25$ MV cm^{-1} (green) and $E = 0.5$ MV cm^{-1} (red). Molecular dynamics simulation data are shown for $E = 0$ MV cm^{-1} (black), $E = 0.3$ MV cm^{-1} (green) and $E = 0.6$ MV cm^{-1} (red). **c**, $Q(f)$ for the bulk-like layers 100–113 (black) and domain-wall layers 73–84 (red), obtained from molecular dynamics simulations at $E = 0.6$ MV cm^{-1}. **d**, Hopping rates for individual layers of the $120 \times 10 \times 10$ supercell for $E = 0$ MV cm^{-1} (black), $E = 0.3$ MV cm^{-1} (green) and $E = 0.6$ MV cm^{-1} (red). **e**, Autocorrelation functions for the total polarization time, obtained from molecular dynamics simulations for $E = 0$ MV cm^{-1} (black), $E = 0.3$ MV cm^{-1} (green) and $E = 0.6$ MV cm^{-1} (red).

domain walls. The strong impact of domain-wall oscillations on the dielectric response and the presence of a high density of domain walls in our sample superdomain state suggest that these oscillations may also be the cause of $Q(f)$ oscillations.

To understand the relationships between the reversible domain-wall dynamics and $Q(f)$, we perform long (14 ns) simulations using a model system containing two aa_1/aa_2 domain walls in a $120 \times 10 \times 10$ supercell (Fig. 3a) at 50 K below the ferroelectric–paraelectric transition temperature and then obtain $Q(f)$ from the fluctuations of the total polarization of the supercell. We choose this size because at this domain length (24 nm) a clear distinction is observed between the domain wall and the bulk-like regions in the sample, as can be seen in Fig. 3a. Additionally, GLD theory predicts that the domain size should be of the order of 30 nm (Supplementary Information).

Comparison of the experimental and molecular-dynamics-obtained $Q(f)$ shows several similar features (Fig. 3b). First, at zero direct current (d.c.) bias, the linear or almost linear rise in Q with decreasing f is succeeded by flattening of $Q(f)$ with gentle oscillations, owing to the onset of relaxation at about 18 GHz (black arrow). This observation is in agreement with the expectation that the presence of domain walls leads to higher loss and lower Q, as can be seen from the much lower Q in the low-f region (less than 2 GHz for the experiment and less than 18 GHz for the molecular dynamics simulation) than that expected from the intrinsic $1/f$ dependence of Q. Second, at higher bias, peaks above the baseline appear at certain frequencies (blue arrows), with the $Q(f)$ curve shifting to higher frequencies with higher d.c. bias. Finally, a greater number of narrow peaks are observed in $Q(f)$ at higher bias. The $Q_y(f)$ results of the molecular dynamics simulations for $E = 0$ MV cm^{-1} and $E = 0.6$ MV cm^{-1} are qualitatively similar to the experimental $Q(f)$ data for $E = 0.09$ MV cm^{-1} and $E = 0.25$ MV cm^{-1}, respectively, albeit at higher frequencies owing to the difference between the experimental BST and the computational BTO systems (Fig. 3b). The uniform shift to higher Q values with higher d.c. bias is not observed for molecular dynamics simulations, and this difference is probably due to the difference between the simple model used in the molecular dynamics simulations and the much more complex E-field profile in the experimental samples.

Analysis of the $Q(f)$ curves of individual layers shows that the bulk-like layers (that is, layers in the middle of the domain that do not show switching) exhibit bulk-like $1/f$ dependence of Q, whereas the domain-wall layers exhibit $Q(f)$ spikes and a flattening out of the $Q(f)$ at low f, similar to the experimentally observed data and the $Q(f)$ obtained computationally for the total system (Fig. 3c). Comparison between the autocorrelation functions of the bulk-like and domain-wall layers (Supplementary Information) shows that the former exhibits the normal behaviour of rapid decay followed by small fluctuations around 0, whereas the latter shows a slow decay and large oscillation amplitude and period. This is due to the much larger fluctuations of the polarization $\boldsymbol{P}$ of the domain-wall layer between the two sides of the double-well potential compared to the oscillations of $\boldsymbol{P}$ inside a well. Therefore, domain-wall fluctuations dominate the dielectric response at low f.

Analysis of the polarization switching (from $-P_y$ to $+P_y$ and vice versa) rates for individual layers in the supercell shows that hopping rates increase with increasing d.c. bias (Fig. 3d), which can also be seen from the oscillations of the autocorrelation functions over the total polarization time (Fig. 3e). Therefore, the application of the d.c. bias accelerates the rate of domain-wall oscillations and leads to the shift of the $Q(f)$ curves to higher f. With no domain-wall oscillations, a bulk-like $1/f$-dependence spectrum is obtained, whereas for slow domain-wall hopping a relaxation-driven flattening of $Q(f)$ is observed with gentle oscillations, and sharp peaks are obtained for faster hopping. This strongly suggests that the experimental $Q(f)$ spectrum with gentle oscillations at zero bias is due to the slow oscillations of the high domain-wall density, and the experimentally observed sharp peaks in $Q(f)$ are due to the acceleration of domain-wall hopping by the application of the d.c. bias.

To show that the domain-wall fluctuation mechanism alone can give rise to the observed sharp $Q(f)$ peaks, we perform stochastic

simulations using a simple model of coupled bistable oscillators with a domain wall (Supplementary Information). We find that domain-wall position oscillations and $Q(f)$ profiles qualitatively similar to those obtained in the molecular dynamics simulations can be obtained by adjusting the double-well parameters of the oscillators (Supplementary Information), demonstrating that domain-wall oscillations can give rise to the observed sharp variation in $Q(f)$. We note that bistable anharmonic oscillators are known to exhibit a variety of resonance behaviours, such as enhanced signal-to-noise ratio at certain frequencies, due to the fluctuation of the system between the two sides of the double well[32]. Thus, the behaviour of the MDVM BST film appears to be another example of this class of phenomena.

The hypothesis that the domain-wall position fluctuations give rise to the anomalous $Q(f)$ observed at high static bias explains why such characteristics have not been previously observed for $Q(f)$. To obtain $Q(f)$ oscillations, a large domain-wall density corresponding to domain size of less than 100 nm is necessary because otherwise the high Q arising from the domain walls will be averaged out by the normal behaviour of the bulk of the domain. In addition, this effect is likely to appear only close to T_C, where the thickness of the domain wall is larger and the barrier to switching is very low, enabling hopping of the domain-wall layer between the two P_y orientations at gigahertz frequencies. At lower T, the energy barrier for switching the P_y value of the layer is too high, so that the time necessary to cross the barrier between the two P_y states is too long; therefore, high Q would be observed only at frequencies in the megahertz range or below, where such an effect may not be apparent owing to the high Q of the bulk dielectric response at such low frequencies. Finally, films of very high quality are necessary to observe these effects, because variation in the frequencies of the very-low-dielectric-loss resonance due to defects, grain boundaries and compositional variations would lead to averaging out of the low loss and disappearance of the high-Q peaks.

The product Qf is one of the most frequently cited metrics for all dielectric microwave resonators, where acoustic attenuation parameterized by $\alpha \propto f^2$ in the Akhiezer limit[33] for phonon–phonon scattering leads to Qf equaling a material-specific constant. We note that in our experimental films, Qf deviates from the usual monotonic $Q(f)$ dependence for 1 GHz $< f_r <$ 10 GHz, showing a strong increase in this range. This suggests that the effective scattering rate due to thermal phonons is much lower than f_r, providing additional experimental evidence that our domain-wall-enhanced resonant films overcome intrinsic losses in this range. Meanwhile, our simulations of BTO indicate that the expected frequency band of voltage-tuned domain-wall resonances is material-specific and can be higher than that experimentally observed for BST. Thus, our results show that extrinsically driven MDVM tunable dielectric materials exhibit a quality factor that exceeds the intrinsic limit near T_C without piezoelectric oscillations, and are promising for achieving similar values of Q at a wider range of frequencies.

Online content

Any Methods, including any statements of data availability and Nature Research reporting summaries, along with any additional references and Source Data files, are available in the online version of the paper at https://doi.org/10.1038/s41586-018-0434-2.

Received: 8 August 2017; Accepted: 26 June 2018;
Published online 20 August 2018.

1. Merz, W. J. Domain formation and domain wall motions in ferroelectric $BaTiO_3$ single crystals. *Phys. Rev.* **95**, 690–698 (1954).
2. Xu, R., Liu, S., Grinberg, I., Karthik, J., Damodaran, A. R., Rappe, A. M. & Martin, L. W. Ferroelectric polarization reversal via successive ferroelastic transitions. *Nat. Mater.* **14**, 79–86 (2015).
3. Chanthbouala, A. et al. Solid-state memories based on ferroelectric tunnel junctions. *Nat. Nanotechnol.* **7**, 101–104 (2012).
4. Muralt, P. Ferroelectric thin films for micro-sensors and actuators: a review. *J. Micromech. Microeng.* **10**, 136–146 (2000).
5. Wessels, B. W. Ferroelectric epitaxial thin films for integrated optics. *Annu. Rev. Mater. Res.* **37**, 659–679 (2007).
6. Arlt, G., Böttger, U. & Witte, S. Dielectric dispersion of ferroelectric ceramics and single crystals at microwave frequencies. *Ann. Phys.* **506**, 578–588 (1994).
7. York, B. in *Multifunctional Adaptive Microwave Circuits and Systems* (eds Steer, M. & Palmer, W. D.) Ch. 6 (SciTech Publishing, Raleigh, 2006).
8. Pertsev, N. A., Zembilgotov, A. G. & Tagantsev, A. K. Effect of mechanical boundary conditions on phase diagrams of epitaxial ferroelectric thin films. *Phys. Rev. Lett.* **80**, 1988–1991 (1998).
9. Lee, C.-H. et al. Exploiting dimensionality and defect mitigation to create tunable microwave dielectrics. *Nature* **502**, 532–536 (2013).
10. Damodaran, A. R., Breckenfeld, E., Chen, Z., Lee, S. & Martin, L. W. Enhancement of ferroelectric Curie temperature in $BaTiO_3$ films via strain-induced defect dipole alignment. *Adv. Mater.* **26**, 6341–6347 (2014).
11. Damodaran, A. R. et al. Nanoscale structure and mechanism for enhanced electromechanical response of highly strained $BiFeO_3$ thin films. *Adv. Mater.* **23**, 3170–3175 (2011).
12. Prosandeev, S., Yang, Y., Paillard, C. & Bellaiche, L. Displacement current in domain walls of bismuth ferrite. *npj Comput. Mater.* **4**, 8 (2018).
13. Wang, Y. L., Tagantsev, A. K., Damjanovic, D. & Setter, N. Giant domain wall contribution to the dielectric susceptibility in $BaTiO_3$. *Appl. Phys. Lett.* **91**, 062905 (2007).
14. Tagantsev, A. K., Sherman, V. O., Astafiev, K. F., Venkatesh, J. & Setter, N. Ferroelectric materials for microwave tunable applications. *J. Electroceram.* **11**, 5–66 (2003).
15. Matzen, S. et al. Super switching and control of in-plane ferroelectric nanodomains in strained thin films. *Nat. Commun.* **5**, 4415 (2014).
16. Griggio, F. et al. Composition dependence of local piezoelectric nonlinearity in $(0.3)Pb(Ni_{0.33}Nb_{0.67})O_3$-$(0.7)Pb(Zr_xTi_{1-x})O_3$ films. *J. Appl. Phys.* **110**, 044109 (2011).
17. Meyers, C. J. G., Freeze, C. R., Stemmer, S. & York, R. A. $(Ba, Sr)TiO_3$ tunable capacitors with RF commutation quality factors exceeding 6000. *Appl. Phys. Lett.* **109**, 112902 (2016).
18. Vorobiev, A., Gevorgian, S., Löffler, M. & Olsson, E. Correlations between microstructure and Q-factor of tunable thin film bulk acoustic wave resonators. *J. Appl. Phys.* **110**, 054102 (2011).
19. Budimir, M., Damjanovic, D. & Setter, N. Extension of the dielectric tunability range in ferroelectric materials by electric bias field antiparallel to polarization. *Appl. Phys. Lett.* **88**, 082903 (2006).
20. Rojac, T., Bencan, A., Drazic, G., Kosec, M. & Damjanovic, D. Piezoelectric nonlinearity and frequency dispersion of the direct piezoelectric response of $BiFeO_3$ ceramics. *J. Appl. Phys.* **112**, 064114 (2012).
21. Zuo, C., Der Spiegel, J. V. & Piazza, G. 1.05-GHz cmos oscillator based on lateral- field-excited piezoelectric AlN contour-mode MEMS resonators. *IEEE Trans. Ultrason. Ferroelectr. Freq. Control* **57**, 82–87 (2010).
22. Gong, S., Kuo, N. K. & Piazza, G. GHz high-Q lateral overmoded bulk acoustic-wave resonators using epitaxial SiC thin film. *J. Microelectromech. Syst.* **21**, 253–255 (2012).
23. Rinaldi, M., Zuniga, C., Zuo, C. & Piazza, G. Super-high-frequency two-port AlN contour-mode resonators for RF applications. *IEEE Trans. Ultrason. Ferroelectr. Freq. Control* **57**, 38–45 (2010).
24. Rinaldi, M., Zuniga, C. & Piazza, G. 5–10 GHz AlN contour-mode nanoelectromechanical resonators. In *2009 IEEE 22nd International Conference on Micro Electro Mechanical Systems* 916–919 (IEEE, 2009).
25. Krupka, J., Tobar, M. E., Hartnett, J. G., Cros, D. & Le Floch, J. M. Extremely high-Q factor dielectric resonators for millimeter-wave applications. *IEEE Trans. Microw. Theory Tech.* **53**, 702–712 (2005).
26. Hartnett, J. G., Tobar, M. E., Ivanov, E. N. & Krupka, J. Room temperature measurement of the anisotropic loss tangent of sapphire using the whispering gallery mode technique. *IEEE Trans. Ultrason. Ferroelectr. Freq. Control* **53**, 34–38 (2006).
27. Magnusson, E. B. et al. Surface acoustic wave devices on bulk ZnO crystals at low temperature. *Appl. Phys. Lett.* **106**, 063509 (2015).
28. Vendik, I. B., Vendik, O. G. & Kollberg, E. L. Commutation quality factor of two-state switchable devices. *IEEE Trans. Microw. Theory Tech.* **48**, 802–808 (2000).
29. Berge, J. & Gevorgian, S. Tunable bulk acoustic wave resonators based on $Ba_{0.25}Sr_{0.75}TiO_3$ thin films and a HfO_2/SiO_2 Bragg reflector. *IEEE Trans. Ultrason. Ferroelectr. Freq. Control* **58**, 2768–2771 (2011).
30. Gevorgian, S. S., Tagantsev, A. K. & Vorobiev, A. K. *Tunable Film Bulk Acoustic Wave Resonators* (Springer, New York, 2013).
31. Hoshina, T. et al. Domain size effect on dielectric properties of barium titanate ceramics. *Jpn. J. Appl. Phys.* **47**, 7607–7611 (2008).
32. Gammaitoni, L., Hänggi, P., Jung, P. & Marchesoni, F. Stochastic resonance. *Rev. Mod. Phys.* **70**, 223–287 (1998).
33. Akhiezer, A. On the absorption of sound in solids. *J. Phys. USSR* **1**, 277 (1939).

Acknowledgements Work at Drexel University and the University of California at Berkeley was supported in part by the US National Science Foundation (NSF) and the Semiconductor Research Corporation under the 'Nanoelectronics in 2020 and Beyond' programme grant number DMR 1124696 and by the Materials Science Division of the US Army Research Office (ARO). Z.G. and G.X. acknowledge support from the ARO under grant number W911NF-14-1-0500. A.P. and A.A.P. acknowledge support from the NSF under grant number IIP 1549668. A.W.-C. acknowledges support from the NSF under grant number DMR 1608887. C.J.H. acknowledges support from the Office of Naval Research under grant number N00014-15-11-2170. J.E.S. acknowledges support from the Air Force Office of Scientific Research under grant number FA9550-13-1-012. I.G., A.S., H.B., J.E.S. and G.X. acknowledge support from the NSF–BSF (US–Israel Binational Science

Foundation) joint programme under grant numbers BSF 2016637 and CBET 1705440. S.P. and A.R.D. acknowledge support from the ARO under grant number W911NF-14-1-0104. A.R.D. also acknowledges the US Department of Energy, Office of Science, Office of Basic Energy Sciences, Materials Sciences and Engineering Division under award number DE-SC-0012375 for the development of the BST materials. A.D. acknowledges support from the NSF under grant number DMR 1708615. S.S. acknowledges support from the NSF under grant number DMR 1608938. L.W.M. acknowledges support from the US Department of Energy, Office of Science, Office of Basic Energy Sciences, Materials Sciences and Engineering Division under contract number DE-AC02-05-CH11231: Materials Project programme KC23MP for the development of new functional materials. R.A.Y. and C.J.G.M. acknowledge support from ARO under grant number W911NF-14-1-0335. Numerical GLD and phase-field simulations were carried out on Proteus, a computer cluster supported by the Drexel University Research Computing Facility.

Reviewer information *Nature* thanks S. Prosandeev, A. Vorobiev and the other anonymous reviewer(s) for their contribution to the peer review of this work.

Author contributions Z.G. and J.E.S. conceived the idea and, together with I.G., proposed the mechanism for high *Q*. Z.G. and J.E.S. developed and implemented the GLD model; G.X., Z.G. and J.E.S. implemented the phase-field model; and A.S., S.L. and I.G. carried out the molecular dynamics simulations and analysis of the molecular dynamics data. H.B. and I.G. developed the stochastic oscillator model. S.P., A.R.D., A.D., Z.G., L.W.M. and J.E.S. designed the growth experiments, and Z.G., I.G. and J.E.S. formulated the interpretation of the experimental data. A.D., A.R.D., S.P. and Z.G. carried out the film synthesis and its optimization. L.W. and P.K.D. produced the solid-state sources. S.P., A.D. and Z.G. carried out X-ray diffraction measurements, X-ray reflectivity analysis and reciprocal space mapping. Z.G., A.D. and S.P. carried out piezoresponse force microscopy analysis. C.J.G.M. designed the microwave devices, carried out film processing and device fabrication and performed microwave measurements and analysis, which were supervised by R.A.Y. Assistance in microwave device design, fabrication, measurements and analysis was provided by A.P., A.A.P. and A.W.-C. The theoretical, experimental and computational modeling aspects of the project were overseen together by I.G., R.A.Y., L.W.M. and J.E.S. All authors contributed to the data analysis. Z.G., I.G. and J.E.S. wrote the manuscript. Z.G., G.X., S.P., A.S., A.D., A.R.D., S.S., C.J.G.M., R.A.Y., I.G., L.W.M. and J.E.S. edited and commented on the manuscript.

Competing interests The authors declare no competing interests.

Additional information
Supplementary information is available for this paper at https://doi.org/10.1038/s41586-018-0434-2.

Correspondence and requests for materials should be addressed to J.E.S.

METHODS

GLD thermodynamic phase and field-dependent susceptibility calculations. Accounting for the self-deformation of BTO and STO to accommodate the BST solid solution[34], the Gibbs free energy density, f_G, includes the Landau energy, f_L, the elastic energy, f_{ela}, and the electrostatic energy, f_{elec}. The total Helmholtz energy, f_{tot}, is obtained through the Lagrange transformation, and the clamped-thin-film boundary condition is applied to eliminate the strain and stress fields. By minimizing f_{tot} with respect to the order parameter polarization, P, the phase diagram is constructed as a function of the temperature, T, and substrate strain, u_s, with the paraelectric, tetragonal, orthorhombic and rhombohedral phases inherited from parent BTO in both single-domain and domain-wall-variant cases. The detailed derivation can be found in Supplementary Information.

Phase field calculations of the polydomains. The domain evolution under external d.c. bias is simulated using a phase-field model. The total free energy density f_{tot} includes the Landau (f_L), electrostriction (f_{es}), elastic (f_{ela}), electrostatic (f_{elec}) and gradient (f_{grad}) contributions. The time-dependent Ginzburg–Landau equation, $d\boldsymbol{P}/dt = -L \times \delta \int f_{tot}\, dV/\delta \boldsymbol{P}$, where L is the kinetic coefficient, is solved in k space with periodic boundary conditions in the film plane and thin-film boundary conditions in the plane normal direction. Details can be found in Supplementary Information.

Pulsed laser deposition. BST targets were prepared by solid-state sintering of commercially available powders. $SmScO_3(110)$ substrates were attached to a heater by silver paste and placed several centrimetres away from the BST target. Substrates were heated to 600 °C, and pulsed laser deposition was carried out using an excimer laser ($\lambda = 248$ nm) with a fluence of around 1.2 J cm^{-2} and a repetition rate of 3 Hz at an O_2 pressure of 20 mtorr. After reaching the expected thickness, the deposition was stopped, an O_2 flow of 1 atm was supplied into the chamber and the films were cooled to room temperature at a rate of 5 °C min^{-1}.

Structural characterizations. X-ray diffraction and reciprocal space mapping about the psuedocubic (103) substrate plane were performed using a Panalytical MRD diffractometer. $\theta/2\theta$ scans (with minor umweg peaks) confirmed phase purity and indicated that each film was strained with the substrate.

Piezoresponse force microscopy. Normal and lateral piezoresponse force microscopy analysis was carried out at room temperature using the DART^{TM} mode as implemented on an Asylum Research MFP-3D scanning probe microscope. Each sample was scanned at 0° and 45° to eliminate the possibility of scan-angle-induced artefacts in the observed patterns.

Fabrication of test structures. Two-port IDC electrodes were fabricated on the samples by a lift-off metallization process using bi-layer photoresist. To begin, the samples were cleaned with ultrasonic agitation in acetone, followed by an isopropanol rinse. The resist stack consisted of 2.2 μm of polydimethylglutarimide (PMGI) polymer topped by 1.8 μm of negative photoresist (AZ nLOF-2020). The PMGI was baked for 5 min at 180 °C and then cooled to 50 °C at 5 °C min^{-1} before the imaging resist was spun, then baked at 110 °C and similarly cooled. The negative imaging resist was exposed through a photomask using projection lithography and developed in tetra-methyl ammonium hydroxide developer. After rinsing in deionized water, the sample was flood-exposed with deep ultraviolet light to scissor the cross-linked PMGI underlayer. The ultraviolet-scissored PMGI underlayer was developed using a tetra-ethyl ammonium hydroxide developer, in which the imaging resist is insoluble, yielding a retrograde profile in the resist sidewall. Finally, 15 nm of Ti was evaporated by electron-beam evaporation as an adhesion layer, followed by 1 μm of Au. The sample was then soaked in 1165 solvent overnight to complete the lift-off.

Microwave radiofrequency measurements. Devices were tested using a two-port microwave setup capable of applying large d.c. bias voltage, illustrated in Fig. 1i. Data were collected for the frequency and voltage dependence of the two-port complex reflection coefficients from 0.1 GHz to 40 GHz in 100-MHz steps and for an applied bias range from −200 V to +200 V (corresponding to $|E| \lesssim 0.67$ MV cm^{-1}). Microwave radiofrequency measurements were performed using a four-port programmable vector network analyser (VNA; Agilent N5227A, 67 GHz) and a Cascade Microtech Summit 9K probe station equipped with 150-μm- and 100-μm-pitch coplanar ground–signal–ground probes (Infinity I67-A-150-GSG-HC, Cascade Microtech). The system was cabled with flexible radiofrequency cables fitted with 1.85-mm V-connectors with a swept right angle at the probe end (4F0BX0BB0240, W.L. Gore and Associates). External high-voltage bias tees attached in-line at the probe heads allowed a d.c. bias voltage, supplied by an external Keithley 2634A source-measurement unit, to be applied to the IDC electrodes during the radiofrequency measurements of the frequency and voltage dependence of the two-port complex reflection coefficients. The measurement system was calibrated using a line–reflect–reflect–match algorithm. The calibration measurements were performed with WinCal XE software from Cascade Microtech using thru, short and 50-Ω-load standards on an impedance standard substrate (101-109C, Cascade Microtech) and an open load standard formed by raising the probe station platen lever to lift the probes to more than 200 μm above the impedance standard substrate. Each frequency sweep was composed of three averaged sweeps with a system (intermediate frequency) bandwidth of 200 Hz, corresponding to a noise floor better than −100 dBm. The VNA power level was set to −15 dBm with a power slope of 0.01 dB GHz^{-1} to compensate for increased cable loss at higher frequencies. When collecting the data, voltage was stepped from zero to 5 V, −5 V, 10 V, −10 V, and so on, to ±200 V. At each bias point, the voltage was held for 5 s before the VNA measurement was triggered. The total applied voltage was divided across the two device ports, referenced to port 1 so that for a given bias V, $V/2$ was applied to port 1 and $-V/2$ was applied to port 2, with polarities inverted for negative bias points (see Supplementary Information).

Molecular dynamics calculations. The simulations were performed in the constant-pressure constant-temperature ensemble using a Nose–Hoover thermostat and a Rahman–Parinello barostat with a 1 fs time step in a $10 \times 10 \times 10$ $BaTiO_3$ supercell (5,000 atoms) for the single-domain calculations and in a $120 \times 10 \times 10$ $BaTiO_3$ supercell (60,000 atoms) for domain simulations. A detailed description of the bond-valence potential is provided elsewhere[35]. Briefly, this potential is parameterized to reproduce density functional theory energies and forces and reproduces the four phases (rhombohedral, orthorhombic, tetragonal and cubic) of $BaTiO_3$. However, owing to the known underestimation of the ferroelectric–paraelectric T_C by density functional theory, the Curie temperature for the bulk bond-valence $BaTiO_3$ is 160 K, and it is 200 K for the strain conditions of the $120 \times 10 \times 10$ domain-wall sample simulations. Therefore, to study the dielectric response of the material in the paraelectric phase (and around T_C), we performed bond-valence molecular-dynamics simulations at 150 K, 160 K, 180 K and 200 K (10 K below T_C, at T_C, and at 20 K and 40 K above T_C, respectively). Once 10 ns of atomic trajectory data were obtained, we calculated the total dipole moment of the simulation supercell using the Born effective charges of the individual atoms and their instantaneous displacements from the high-symmetry positions. The total dipole moment was then used to calculate the autocorrelation function, which was then Fourier-transformed to obtain the real (ε_r) and imaginary (ε_{imag}) components of the dielectric constant and the quality factor.

Calculation of the hopping rates. To evaluate the average hopping rate of the average polarization of a layer in the xy plane in our supercell, we count the number of times, N, that the average polarization of the layer switched from a positive value at time t to a negative value at time $t + \delta t$, where $\delta t = 0.5$ ps is the interval between the printing of the atomic coordinates during the simulation. Because the total simulation time is 10 ns, the average rate of $\boldsymbol{P}$ switching for the layer is $N/10$ ns^{-1} or $N/10$ GHz. This corresponds to the hopping rate of the layer between the two sides of the potential energy well.

Data availability. Data are available from the corresponding author upon reasonable request.

34. Shirokov, V. B., Yuzkuk, Yu. I., Dkhil, B. & Lemanov, V. V. Phenomenological theory of phase transitions in epitaxial $Ba_xSr_{1-x}TiO_3$ thin films. *Phys. Rev. B* **79**, 144118 (2009).
35. Qi, Y., Liu, S., Grinberg, I. & Rappe, A. M. Atomistic description for temperature-driven phase transitions in $BaTiO_3$. *Phys. Rev. B* **94**, 134308 (2016).